submitted to *Geophys. J. Int.*

A new earthquake location method based on the waveform inversion

Hao Wu[1], Jing Chen[1], Xueyuan Huang[2], and Dinghui Yang[1]

[1] *Department of Mathematical Sciences, Tsinghua University, Beijing, China. E-mail: dhyang@math.tsinghua.edu.cn*

[2] *Department of Mathematics, School of Science, Beijing Technology and Business University, Beijing, China.*

arXiv:1610.07135v1 [math.NA] 23 Oct 2016

SUMMARY

In this paper, a new earthquake location method based on the waveform inversion is proposed. As is known to all, the waveform misfit function is very sensitive to the phase shift between the synthetic waveform signal and the real waveform signal. Thus, the convergence domain of the conventional waveform based earthquake location methods is very small. In present study, by introducing and solving a simple sub-optimization problem, we greatly expand the convergence domain of the waveform based earthquake location method. According to a large number of numerical experiments, the new method expands the range of convergence by several tens of times. This allows us to locate the earthquake accurately even from some relatively bad initial values.

Key words: Computational seismology; Inverse theory; Numerical modelling; Waveform inversion.

1 INTRODUCTION

The earthquake location is a fundamental problem in seismology (Ge 2003a; Thurber 2014). It consists of two parts: the determination of hypocenter $\boldsymbol{\xi}$ and origin time τ. These information are extremely important in quantitative seismology, e.g. the earthquake early warning system (Satriano et al. 2008), the investigation of seismic heterogeneous structure (Tong et al. 2016; Waldhauser &

Ellsworth 2000). In particular, there are also significant interests in micro-earthquake which has many applications in exploration seismology (Lee & Stewart 1981; Prugger & Gendzwill 1988).

Due to the importance of the earthquake location problem, numerous studies have been done theoretically and experimentally, see e.g. (Ge 2003a; Ge 2003b; Geiger 1910; Geiger 1912; Milne 1986; Prugger & Gendzwill 1988; Thurber 1985). However, many studies are based on the ray theory, which has low accuracy when the wave length is not small enough compared to the scale of wave propagating region (Engquist & Runborg 2003; Jin et al. 2008; Jin et al. 2011; Liu et al. 2013; Rawlinson et al. 2010; Wu & Yang 2013). This may lead to inaccurate or even incorrect earthquake location results. An alternative way is to solve the wave equation directly to get accurate information for inversion. This method is becoming popular in recent years, as a result of the fast increasing computational power (Huang et al. 2016; Kim et al. 2011; Liu & Gu 2012; Liu et al. 2004; Tape et al. 2007; Tong et al. 2014a; Tong et al. 2014b; Tong et al. 2014c).

In the work by (Liu et al. 2004), see also (Kim et al. 2011), the spectral-element solvers are implemented to invert the basic information of earthquakes. The misfit functions defined based upon the envelope of the waveforms are minimized to provide the best estimation of source model parameters. Another approach proposed by (Tong et al. 2016) is based on the wave-field relation between the hypocenter $\boldsymbol{\xi}$ and its perturbation $\boldsymbol{\xi} + \delta\boldsymbol{\xi}$ (Alkhalifah 2010). Due to the foregoing observation, the travel-time differences between the synthetic single and the real single can be approximately expressed as the linear function of hypocenter perturbation $\delta\boldsymbol{\xi}$. The authors then derived the sensitivity kernel by using the forward and adjoint wavefields.

However, the above mentioned papers on the earthquake location are not directly used the waveform difference since the waveform misfit function is very sensitive to the phase shift between the synthetic waveform signal and the real waveform signal (Liu et al. 2004). Consider the bad mathematical properties of the delta function $f(t-\tau)\delta(\boldsymbol{x}-\boldsymbol{\xi})$, who is appeared as the source of wave equation, even small perturbation of hypocenter $\delta\boldsymbol{\xi}$ and origin time $\delta\tau$ would generate large deviation of waveform. Thus, it is not surprising that the range of convergence of the conventional waveform based method is very small. On the other hand, the waveform signal may contain more

information, which could lead to more accurate location result. Thus, it is necessary to develop new techniques to expand the convergence domain of the waveform based location method.

In this paper, we present a new method to locate the earthquake accurately. For the sake of simplicity, we use the acoustic wave equation and only deal with the earthquake hypocenter and origin time. There is no essential difficulty to consider the elastic wave equation or involve more earthquake information, e.g. the moment magnitudes (Liu et al. 2004). The starting point is to keep $\frac{\|\delta s(\boldsymbol{x},t)\|}{\|s(\boldsymbol{x},t)\|} \ll 1$ in a modified sense. This is a fundamental assumption of the first-order Born approximation in the adjoint method. But it is not easy to guarantee in the classical sense, even if $\frac{\|\delta \boldsymbol{\xi}\|}{\|\boldsymbol{\xi}\|}$ and $\frac{\|\delta \tau\|}{\|\tau\|}$ are small. This is due to the bad mathematical properties of the delta function $f(t-\tau)\delta(\boldsymbol{x}-\boldsymbol{\xi})$ in the wave equation. To solve this problem, we shift the synthetic data so that its difference with the real data is minimized. The shifting parameter can be obtained by solving a simple sub-optimization problem. The above effects ensure correctness of the important assumption $\frac{\|\delta s(\boldsymbol{x},t)\|}{\|s(\boldsymbol{x},t)\|} \ll 1$ of the adjoint method in a large range. Thus, we can expect a large convergence domain of the new earthquake location method. According to the numerical experiments, the range of convergence is significantly enlarged. We also remark that the idea is similar to the Wasserstein metric (Engquist & Froese 2014; Engquist et al. 2016), but we provide a simple and alternative implementation.

The paper is organized as follows. In Section 2, the conventional waveform based adjoint inversion method is reviewed for the earthquake hypocenter and origin time. We propose the new method for the earthquake location in Section 3. In Section 4, the numerical experiments are provided to demonstrate the effectiveness of the new method. Finally, we make some conclusive remarks in Section 5.

2 THE INVERSION METHOD

Consider the scalar acoustic wave equation

$$\frac{\partial^2 u(\boldsymbol{x},t;\boldsymbol{\xi},\tau)}{\partial t^2} = \nabla\cdot\big(c^2(\boldsymbol{x})\nabla u(\boldsymbol{x},t;\boldsymbol{\xi},\tau)\big) + f(t-\tau)\delta(\boldsymbol{x}-\boldsymbol{\xi}), \quad \boldsymbol{x},\boldsymbol{\xi}\in\Omega, \tag{1}$$

with initial-boundary conditions

$$u(\boldsymbol{x}, 0; \boldsymbol{\xi}, \tau) = \partial_t u(\boldsymbol{x}, 0; \boldsymbol{\xi}, \tau) = 0, \quad \boldsymbol{x} \in \Omega, \tag{2}$$

$$\boldsymbol{n} \cdot \left(c^2(\boldsymbol{x}) \nabla u(\boldsymbol{x}, t; \boldsymbol{\xi}, \tau)\right) = 0, \quad \boldsymbol{x} \in \partial\Omega. \tag{3}$$

Here $u(\boldsymbol{x}, t; \boldsymbol{\xi}, \tau)$ is the wavefield with respect to parameters τ and $\boldsymbol{\xi}$. The wave speed is $c(\boldsymbol{x})$. The simulated domain $\Omega \subset \mathbb{R}^d$, d is the dimension of the problem and $\boldsymbol{n}$ is the unit outer normal vector to the boundary $\partial\Omega$ of Ω. The seismogram at source has the form of Ricker wavelet

$$f(t) = A\left(1 - 2\pi^2 f_0^2 t^2\right) e^{-\pi^2 f_0^2 t^2},$$

in which f_0 is the dominant frequency and A is the normalization factor. In this study, the point source hypothesis $\delta(\boldsymbol{x} - \boldsymbol{\xi})$ for the hypocenter focus is considered for the situation where the temporal and spatial scales of seismic rupture are extremely small compared to the scales of seismic waves propagated (Aki & Richards 1980; Madariaga 2015). For simplicity, the reflection boundary condition (3) is considered here. There is no essential difference for other boundary conditions, e.g. the perfectly matched layer absorbing boundary condition (Komatitsch & Tromp 2003; Ma et al. 2015).

Remark 2.1. For the acoustic wave equation (1), we have the invariance property in time translation (Evans 2010)

$$u(\boldsymbol{x}, t - \Delta\tau; \boldsymbol{\xi}, \tau) = u(\boldsymbol{x}, t; \boldsymbol{\xi}, \tau + \Delta\tau). \square$$

Remark 2.2. The compatibility condition requires that

$$f(t - \tau) = 0 \text{ and } \tau > 0.$$

These are very nature in practical problems. □

Let $\boldsymbol{\xi}_T$ and τ_T be the real earthquake hypocenter and origin time. Thus, the real earthquake signal $d_r(t)$, which was receiver at station r can be considered as

$$d_r(t) = u(\boldsymbol{\eta}_r, t; \boldsymbol{\xi}_T, \tau_T). \tag{4}$$

Here $\boldsymbol{\eta}_r$ is the location of the $r-$th receiver. The synthetic signal $s(\boldsymbol{x},t)$ corresponding to the initial hypocenter $\boldsymbol{\xi}$ and origin time τ is

$$s(\boldsymbol{x},t) = u(\boldsymbol{x},t;\boldsymbol{\xi},\tau). \tag{5}$$

By introducing the misfit function

$$\chi_r(\boldsymbol{\xi},\tau) = \frac{\int_0^T |d_r(t) - s(\boldsymbol{\eta}_r,t)|^2 \,\mathrm{d}t}{2\int_0^T |d_r(t)|^2 \,\mathrm{d}t}, \tag{6}$$

we define the nonlinear optimization problem

$$(\boldsymbol{\xi}_T,\tau_T) = \underset{\boldsymbol{\xi},\,\tau}{\operatorname{argmin}} \sum_r \chi_r(\boldsymbol{\xi},\tau). \tag{7}$$

Obviously, the global solution exists and is unique (Nocedal & Wright 1999). In the following part, the sensitivity kernel (Liu & Gu 2012; Rawlinson et al. 2010; Tong et al. 2014b) will be derived to solve this inversion problem iteratively.

2.1 The adjoint method

The perturbation of parameters $\frac{\|\delta\boldsymbol{\xi}\|}{\|\boldsymbol{\xi}\|}$ and $\frac{\|\delta\tau\|}{\|\tau\|} \ll 1$ would generate the perturbation of wave function $\delta s(\boldsymbol{x},t)$, it writes

$$\delta s(\boldsymbol{x},t) = u(\boldsymbol{x},t;\boldsymbol{\xi}+\delta\boldsymbol{\xi},\tau+\delta\tau) - u(\boldsymbol{x},t;\boldsymbol{\xi},\tau).$$

Then $\delta s(\boldsymbol{x},t)$ satisfies

$$\begin{cases} \frac{\partial^2 \delta s(\boldsymbol{x},t)}{\partial t^2} = \nabla\cdot(c^2(\boldsymbol{x})\nabla\delta s(\boldsymbol{x},t)) + f(t-(\tau+\delta\tau))\delta(\boldsymbol{x}-(\boldsymbol{\xi}+\delta\boldsymbol{\xi})) - f(t-\tau)\delta(\boldsymbol{x}-\boldsymbol{\xi}), & \boldsymbol{x}\in\Omega, \\ \delta s(\boldsymbol{x},0) = \frac{\partial \delta s(\boldsymbol{x},0)}{\partial t} = 0, & \boldsymbol{x}\in\Omega, \\ \boldsymbol{n}\cdot(c^2(\boldsymbol{x})\nabla\delta s(\boldsymbol{x},t)) = 0, & \boldsymbol{x}\in\partial\Omega. \end{cases} \tag{8}$$

Multiply an arbitrary test funciton $w_r(\boldsymbol{x},t)$ on equation (8), integrate it on $\Omega\times[0,T]$ and use integration by parts, we obtain

$$\begin{aligned}
&\int_0^T\int_\Omega \frac{\partial^2 w_r}{\partial t^2}\delta s\mathrm{d}\boldsymbol{x}\mathrm{d}t-\int_\Omega \frac{\partial w_r}{\partial t}\delta s\Big|_{t=T}\mathrm{d}\boldsymbol{x}+\int_\Omega w_r\frac{\partial \delta s}{\partial t}\Big|_{t=T}\mathrm{d}\boldsymbol{x}\\
&\qquad=\int_0^T\int_\Omega \delta s\nabla\cdot(c^2\nabla w_r)\mathrm{d}\boldsymbol{x}\mathrm{d}t-\int_0^T\int_{\partial\Omega}\boldsymbol{n}\cdot(c^2\nabla w_r)\delta s\mathrm{d}\zeta\mathrm{d}t\\
&\qquad\quad+\int_0^T f(t-(\tau+\delta\tau))w_r(\boldsymbol{\xi}+\delta\boldsymbol{\xi},t)-f(t-\tau)w_r(\boldsymbol{\xi},t)\mathrm{d}t\\
&\qquad\approx\int_0^T\int_\Omega \delta s\nabla\cdot(c^2\nabla w_r)\mathrm{d}\boldsymbol{x}\mathrm{d}t-\int_0^T\int_{\partial\Omega}\boldsymbol{n}\cdot(c^2\nabla w_r)\delta s\mathrm{d}\zeta\mathrm{d}t\\
&\qquad\qquad+\int_0^T f(t-\tau)\nabla w_r(\boldsymbol{\xi},t)\cdot\delta\boldsymbol{\xi}-f'(t-\tau)w_r(\boldsymbol{\xi},t)\delta\tau\mathrm{d}t. \quad (9)
\end{aligned}$$

Note that the Taylor expansion is used and higher order terms is ignored in the last step.

On the other hand, the misfit function (6) also generates the perturbation with respect to $\delta s(\boldsymbol{x},t)$, assume that $\frac{\|\delta s(\boldsymbol{x},t)\|}{\|s(\boldsymbol{x},t)\|}\ll 1$, it writes

$$\begin{aligned}
\delta\chi_r&=\chi_r(\boldsymbol{\xi}+\delta\boldsymbol{\xi},\tau+\delta\tau)-\chi_r(\boldsymbol{\xi},\tau)\\
&=\frac{\int_0^T\left(|d_r(t)-(s+\delta s)(\boldsymbol{\eta}_r,t)|^2-|d_r(t)-s(\boldsymbol{\eta}_r,t)|^2\right)\mathrm{d}t}{2\int_0^T|d_r(t)|^2\,\mathrm{d}t}\\
&\approx-\frac{\int_0^T(d_r(t)-s(\boldsymbol{\eta}_r,t))\delta s(\boldsymbol{\eta}_r,t)\mathrm{d}t}{\int_0^T|d_r(t)|^2\,\mathrm{d}t}\\
&=-\frac{\int_0^T\int_\Omega(d_r(t)-s(\boldsymbol{\eta}_r,t))\delta s(\boldsymbol{x},t)\delta(\boldsymbol{x}-\boldsymbol{\eta}_r)\mathrm{d}\boldsymbol{x}\mathrm{d}t}{\int_0^T|d_r(t)|^2\,\mathrm{d}t}, \quad (10)
\end{aligned}$$

where "$\approx$" is obtained by ignoring high order terms of $\delta s(\boldsymbol{x},t)$.

Let $w_r(\boldsymbol{x},t)$ satisfy the wave equation with terminal-boundary conditions

$$\begin{cases}
\frac{\partial^2 w_r(\boldsymbol{x},t)}{\partial t^2}=\nabla\cdot(c^2(\boldsymbol{x})\nabla w_r(\boldsymbol{x},t))+\frac{d_r(t)-s(\boldsymbol{\eta}_r,t)}{\int_0^T|d_r(t)|^2\mathrm{d}t}\delta(\boldsymbol{x}-\boldsymbol{\eta}_r), & \boldsymbol{x}\in\Omega,\\
w_r(\boldsymbol{x},T)=\frac{\partial w_r(\boldsymbol{x},T)}{\partial t}=0, & \boldsymbol{x}\in\Omega,\\
\boldsymbol{n}\cdot(c^2(\boldsymbol{x})\nabla w_r(\boldsymbol{x},t))=0, & \boldsymbol{x}\in\partial\Omega.
\end{cases} \quad (11)$$

Thus, the linear relation for $\delta\chi$ and $\delta\boldsymbol{\xi},\ \delta\tau$ can be obtained by subtracting (10) from (9)

$$-\delta\chi_r=\int_0^T f(t-\tau)\nabla w_r(\boldsymbol{\xi},t)\cdot\delta\boldsymbol{\xi}-f'(t-\tau)w_r(\boldsymbol{\xi},t)\delta\tau\mathrm{d}t. \quad (12)$$

In particular, if

$$\boldsymbol{\xi}+\delta\boldsymbol{\xi}=\boldsymbol{\xi}_T,\ \tau+\delta\tau=\tau_T,$$

it implies

$$\chi_r(\boldsymbol{\xi}+\delta\boldsymbol{\xi},\tau+\delta\tau)=0 \;\Rightarrow\; \delta\chi_r=-\chi_r(\boldsymbol{\xi},\tau).$$

This gives an alternative form of equation (12)

$$\chi_r(\boldsymbol{\xi},\tau)=\int_0^T f(t-\tau)\nabla w_r(\boldsymbol{\xi},t)\cdot\delta\boldsymbol{\xi}-f'(t-\tau)w_r(\boldsymbol{\xi},t)\delta\tau\mathrm{d}t. \tag{13}$$

By defining the sensitivity kernel for the hypocenter $\boldsymbol{\xi}$ and origin time τ as

$$K_r^{\boldsymbol{\xi}}=\int_0^T \nabla w_r(\boldsymbol{\xi},t)f(t-\tau)\mathrm{d}t,$$
$$K_r^{\tau}=-\int_0^T w_r(\boldsymbol{\xi},t)f'(t-\tau)\mathrm{d}t,$$

equation (13) gives a single equation of the large linear system

$$\frac{K_r^{\boldsymbol{\xi}}}{\chi_r(\boldsymbol{\xi},\tau)}\cdot\delta\boldsymbol{\xi}+\frac{K_r^{\tau}}{\chi_r(\boldsymbol{\xi},\tau)}\delta\tau=1. \tag{14}$$

The above linear system has been nomailized so that the condition number can be optimized

3 A NEW METHOD TO EXPAND THE CONVERGENCE DOMAIN

In this section, we are investigating the techniques to enlarge the convergence domain for the inversion of earthquake hypocenter $\boldsymbol{\xi}_T$ and origin time τ_T. It is assumed that the wave speed $c(\boldsymbol{x})$ is already well known. For situations of inaccurate or unknown wave speed, we refer to the discussions in (Liu et al. 2004) or the joint inversion for wave speed, hypocenter and origin time.

3.1 Estimation of the origin time

As it was discussed in Section 2.1, the first-order Born approximation in the adjoint method requires an infinitesimal perturbation assumption of wave function

$$\frac{\|\delta s(\boldsymbol{x},t)\|}{\|s(\boldsymbol{x},t)\|}\ll 1,$$

see also (Liu & Gu 2012; Rawlinson et al. 2010; Tong et al. 2014b; Tromp et al. 2005). However, as we will see in Example 3.1, it is very difficult to guarantee this assumption even if the perturbations

of the earthquake hypocenter and origin time are very small

$$\frac{\|\delta\boldsymbol{\xi}\|}{\|\boldsymbol{\xi}\|} \ll 1 \text{ and } \frac{\|\delta\tau\|}{\|\tau\|} \ll 1.$$

That's one of the reasons why the convergence domain of the waveform based method is very small.

Example 3.1. This is a 2D unbounded problem with constant wave speed $c(\boldsymbol{x}) \equiv c_0$ for the scalar acoustic wave equation (1) with initial condition (2). Its solution can be analytically given (Evans 2010):

$$u(\boldsymbol{x}, t; \boldsymbol{\xi}, \tau) = \begin{cases} \frac{1}{2\pi c_0^2} \int_0^{\theta_0} \frac{f(\theta-\tau)}{\sqrt{(t-\theta)^2-(t-\theta_0)^2}} \mathrm{d}\theta, & \theta_0 > 0, \\ 0, & \theta_0 \leq 0, \end{cases} \tag{15}$$

in which

$$\theta_0 = t - \frac{1}{c_0} \|\boldsymbol{x} - \boldsymbol{\xi}\|_2 .$$

Let $\boldsymbol{x} = (x, z)$ denote the horizontal and depth coordinate respectively. The constant wave speed is $c_0 = 6.5km/s$. There are 20 equidistant receivers on the surface,

$$\boldsymbol{\eta}_r = (x_r, z_r) = (5r - 2.5km, 0), \quad r = 1, 2, \cdots, 20.$$

Consider an earthquake occurs at hypocenter $\boldsymbol{\xi}_T = (50km, -30km)$ and origin time $\tau_T = 10s$ with dominant frequency $f_0 = 2$Hz, its signal $d_r(t)$ received by station $r = 7$ can be considered as (4) and (15). The synthetic signal $s(\boldsymbol{\eta}_r, t)$ corresponding to the initial hypocenter $\boldsymbol{\xi} = (52km, -30.3km)$ and origin time $\tau = 10s$ at the same station $r = 7$ can be obtained by (5) and (15). The perturbation between the real and initial hypocenter is small

$$\delta\boldsymbol{\xi} = \boldsymbol{\xi}_T - \boldsymbol{\xi} = (-2km, 0.3km),$$

and it is also correct for the perturbation between the real and initial origin time

$$\delta\tau = \tau_T - \tau = 0.$$

Nevertheless, as we can see in Figure 1, the difference between the real signal $d_r(t)$ and the synthetic signal $s(\boldsymbol{\eta}_r, t)$ at receiver station $r = 7$ is significantly large:

$$\frac{\|d_r(t) - s(\boldsymbol{\eta}_r, t)\|}{\|d_r(t)\|} \sim 1,$$

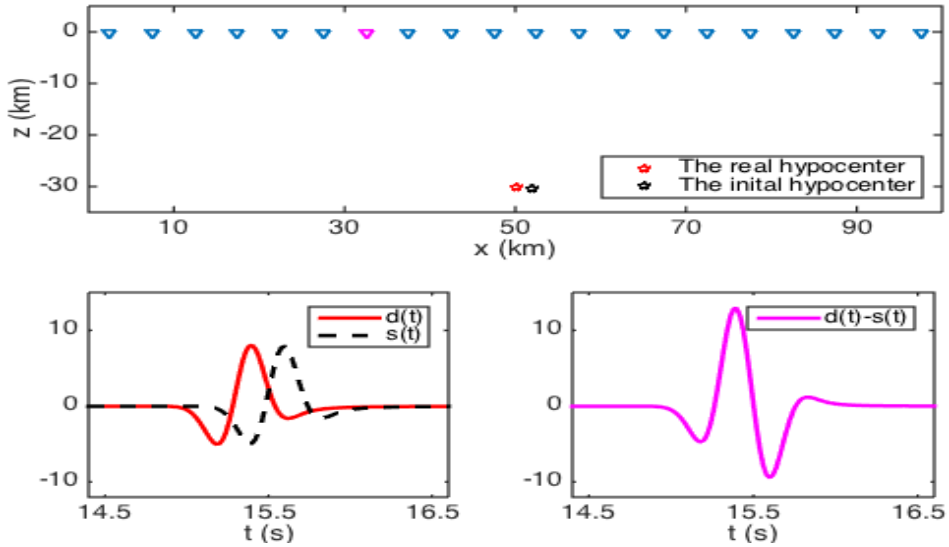

Figure 1. Illustration of Exam 3.1. Up: The receiver stations (up triangle, magenta for $r = 7$ and blue for others), the real (red pentagram) and initial hypocenter (black pentagram). Bottom Left: The real signal $d_r(t)$ (red solid line) and the synthetic signal $s(\boldsymbol{\eta}_r, t)$ (black dashed line) at receiver station $r = 7$. Bottom Right: The difference between the real and synthetic signal $d_r(t) - s(\boldsymbol{\eta}_r, t)$ (magenta solid line) at receiver station $r = 7$. The text representation in the figure has been simplified without causing any misunderstandings.

which contracts to the basic assumption. □

The key observation in Exam 3.1 is that the infinitesimal perturbation assumption $\frac{\|\delta s(\boldsymbol{x},t)\|}{\|s(\boldsymbol{x},t)\|} \ll 1$ is not trivial to get. However, we note that the main difference between the real signal $d_r(t)$ and synthetic signal $s(\boldsymbol{\eta}_r, t)$ is caused by the time shift. Thus, we define the relative error function with respect to the time shift of the synthetic signal

$$e_r(\tau) = \frac{\|d_r(t) - s(\boldsymbol{\eta}_r, t - \tau)\|}{\|d_r(t)\|}. \tag{16}$$

Solving the following sub-optimization problem

$$\tau_r^* = \underset{\tau}{\operatorname{argmin}}\, e_r(\tau), \tag{17}$$

the infinitesimal perturbation assumption may be satisfied in the sense of time translation.

$$\frac{\|d_r(t) - s(\boldsymbol{\eta}_r, t - \tau_r^*)\|}{\|d_r(t)\|} \ll 1, \tag{18}$$

Example 3.2. Consider the same parameters set up as in Exam 3.1, thereby the real signal $d_r(t)$ and the synthetic signal $s(\boldsymbol{\eta}_r, t)$ are the same as those in Exam 3.1.

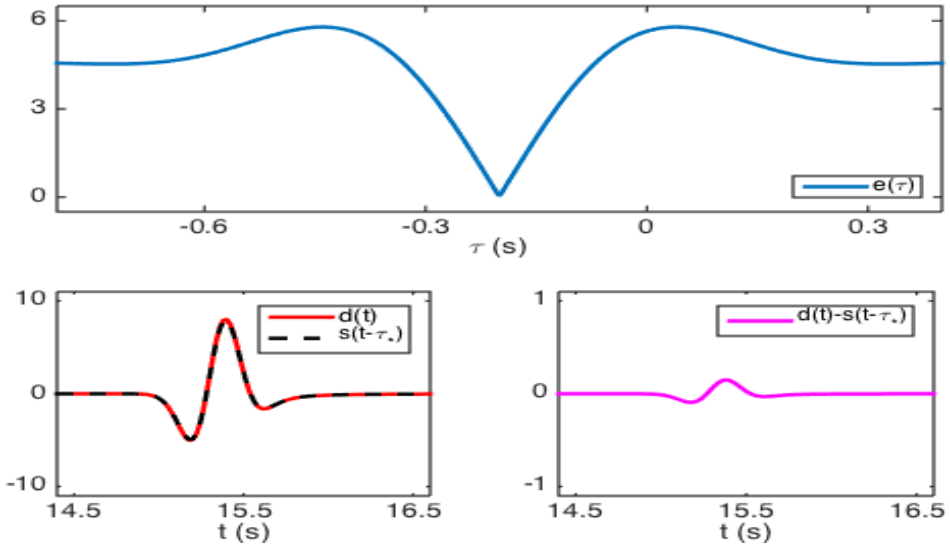

Figure 2. Illustration of Exam 3.2. Up: The relative error function $e_r(\tau)$ defined in (16). Bottom Left: The real signal $d_r(t)$ (red solid line) and the shifted synthetic signal $s(\boldsymbol{\eta}_r, t-\tau_r^*)$ (black dashed line) at receiver station $r=7$. Bottom Right: The difference between the real signal and the shifted synthetic signal $d_t(t)-s(\boldsymbol{\eta}_r, t-\tau_r^*)$ (magenta solid line) at receiver station $r=7$. The text representation in the figure has been simplified without causing any misunderstandings.

The relative error function $e_r(\tau)$ defined in (16) is presented in Figure 2 Up. We can observe a global minimum of $e_r(\tau)$. Thus, the optimal time translation parameter τ_r^* can be easily computed through (17).

According to the above time translation, the difference between the real signal $d_r(t)$ and the shifted synthetic signal $s(\boldsymbol{\eta}_r, t-\tau_r^*)$ is small, see Figure 2 Bottom. This implies that the modified infinitesimal perturbation assumption in (18) is satisfied here. □

At last, by the invariance property in time translation, see Remark 2.1, this optimal time shift τ_r^* computed from (17) can be used to shift the initial origin time

$$\hat{\tau} = \tau + \tau_r^*, \tag{19}$$

so that the infinitesimal perturbation assumption $\frac{\|\delta s(\boldsymbol{x},t)\|}{\|s(\boldsymbol{x},t)\|} \ll 1$ can be satisfied in the original sense rather than the modified sense (18).

Example 3.3. Consider the same parameters set up as in Exam 3.1, thereby the real signal $d_r(t)$ is the same as in Exam 3.1. The synthetic signals are corresponding to the initial hypocenter $\boldsymbol{\xi} = (52km, -30.3km)$ and two different initial origin time: (1) $\tau_1 = 10$s, (2) $\tau_2 = \tau_1 + \tau_r^*$. We

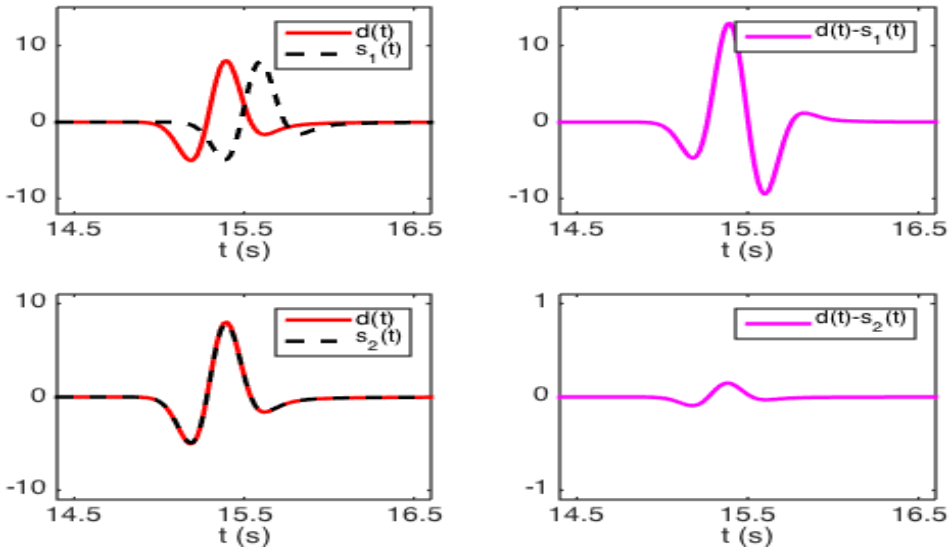

Figure 3. Illustration of Exam 3.3. Left: The real signal $d_r(t)$ (red solid line) and the synthetic signal $s_i(t, \boldsymbol{\eta}_r)$ (black dashed line) at receiver station $r = 7$. Right: The difference between the real signal and the synthetic signal $d_r(t) - s_i(\boldsymbol{\eta}_r, t)$ (magenta solid line) at receiver station $r = 7$. Up: $i = 1$, which corresponding to the initial origin time τ_1. Bottom: $i = 2$, which correspoding to the other initial origin time τ_2. The text representation in the figure has been simplified without causing any misunderstandings.

still focus on the signals received at station $r = 7$. These synthetic signals can be obtained by

$$s_1(\boldsymbol{\eta}_r, t) = u(\boldsymbol{\eta}_r, t; \boldsymbol{\xi}, \tau_1), \quad s_2(\boldsymbol{\eta}_r, t) = u(\boldsymbol{\eta}_r, t; \boldsymbol{\xi}, \tau_2).$$

In Figure 3 Up, the difference between the real signal $d_r(t)$ and the synthetic signal $s_1(\boldsymbol{\eta}_r, t)$ is large, but the difference between the real signal $d_r(t)$ and the other synthetic signal $s_2(\boldsymbol{\eta}_r, t)$ is small, see Figure 3 Bottom. □

3.2 The selection of receiver stations

In previous subsection, the time shift τ_r^* has been discussed for single receiver station r. For practical problems, there are many receiver stations, thus we need to solve the following sub-optimization problem

$$\tau^* = \operatorname*{argmin}_{\tau} \sum_{r \in \mathcal{R}} e_r(\tau), \tag{20}$$

rather than (17). Here $\mathcal{R}$ is the set of all receiver stations that we use for inversion, which will be determined later. The set of all receiver stations is denote by $\mathcal{A}$, and it is obviously that $\mathcal{R} \subset \mathcal{A}$.

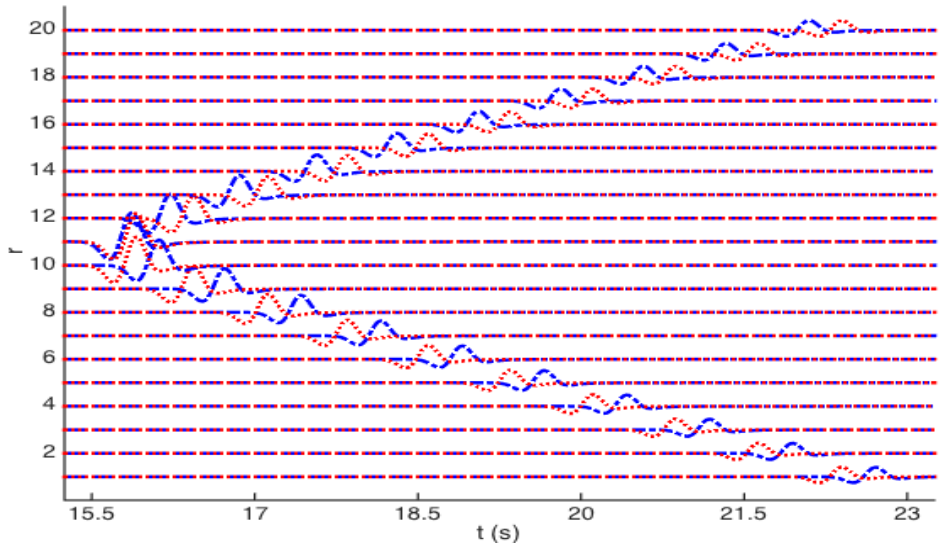

Figure 4. Illustration of Exam 3.4. The waveform comparison of real signals $d_r(t)$ (red dotted line) and the synthetic signals $s(\boldsymbol{\eta}_r, t)$ (blue dashdot line) for all receivers $r = 1, 2, \cdots, 20$. The horizontal axis is the time t, and the longitudinal axis is the index of receiver r.

Example 3.4. Consider the same parameters set up as in Exam 3.1, thereby the real signals $d_r(t)$ and the synthetic signals $s(\boldsymbol{\eta}_r, t)$ can be obtained in the same manner as in Exam 3.1

$$d_r(t) = u(\boldsymbol{\eta}_r, t; \boldsymbol{\xi}_T, \tau_T), \quad s(\boldsymbol{\eta}_r, t) = u(\boldsymbol{\eta}_r, t; \boldsymbol{\xi}, \tau)$$

for all receiver stations $r \in \mathcal{A} = \{1, 2, \cdots, 20\}$. In Figure 4, we output all the real signals $d_t(t)$ and the synthetic signals $s(\boldsymbol{\eta}_r, t)$. According to the figures, we can see that

$$\tau_r^* < 0, \text{ for } r = 1, 2, \cdots, 10,$$

$$\tau_r^* > 0, \text{ for } r = 11, 12, \cdots, 20.$$

Therefore, we cannot get satisfactory value τ^* from (20) if $\#\mathcal{R}$ is large. Here $\#\mathcal{R}$ denotes the number of elements in the set $\mathcal{R}$. □

The above example shows that discussions in Subsection 3.1 may fail when $\#\mathcal{R}$ is large. In fact, due to the small degree of freedom of the earthquake location problem, it is not necessary to consider large $\#\mathcal{R}$. On the other hand, $\#\mathcal{R}$ is the number of constraints, which is proportional to the number of wave field computations. Therefore, we prefer to choose a relative small $\#\mathcal{R}$ for inversion. Accordingly to our numerical experiences, a suitable choice of $\#\mathcal{R}$ is $5 \sim 7$. However, this discussion doesn't determine which elements should be in $\mathcal{R}$. A natural consideration is to

solve a more general nonlinear optimization problem

$$(\tau^*, \mathcal{R}^*) = \underset{\tau,\, \mathcal{R}\subset\mathcal{A}}{\operatorname{argmin}} \sum_{r\in\mathcal{R}} e_r(\tau). \tag{21}$$

The essence of the above problem is that receivers set $\mathcal{R}$ is considered as optimization variable. It is easy to check that for $1 \le n_1 < n_2 \le \#\mathcal{A}$, we have

$$\min_{\tau,\, \#\mathcal{R}=n_1,\, \mathcal{R}\subset\mathcal{A}} \sum_{r\in\mathcal{R}} e_r(\tau) \le \min_{\tau,\, \#\mathcal{R}=n_2,\, \mathcal{R}\subset\mathcal{A}} \sum_{r\in\mathcal{R}} e_r(\tau).$$

In practice, solving the problem (21) is complicated. Instead, we can firstly solve a simplified optimization problem

$$(\bar{\tau}, \mathcal{R}^*) = \underset{\tau,\, \mathcal{R}\subset\mathcal{A}}{\operatorname{argmin}} \sum_{r\in\mathcal{R}} \left|\tau_r^* - \tau\right|^2. \tag{22}$$

Then, for fixed receivers set $\mathcal{R}^*$, we have

$$\tau^* = \underset{\tau}{\operatorname{argmin}} \sum_{r\in\mathcal{R}^*} e_r(\tau). \tag{23}$$

Similar to equation (19), the optimal time shift τ^* for multiple receivers can also be used to shift the initial origin time

$$\hat{\tau} = \tau + \tau^*. \tag{24}$$

3.3 The detailed implementation

In summary of all the above, the detailed implementation of the algorithm is as follows:

1. Initialization. Set the tolerance value $\varepsilon = 0.01km$, the threshold value $\sigma = 100km$ and the break-off step $K = 30$. Let $k = 0$ and give the initial hypocenter $\boldsymbol{\xi}_0$ and the initial origin time $\tau_0 = 0$.
2. For $\boldsymbol{\xi}_k$, solving (22) to determine the receivers set $\mathcal{R}_k^*$ and estimating the origin time τ_k by (23) and (24).
3. Construct the sensitivity kernels $K_{r,k}^{\boldsymbol{\xi}},\ K_{r,k}^{\tau}$ for $r \in \mathcal{R}_k^*$ and solve the normalized linear system (14) to get $\delta\boldsymbol{\xi}_k$ and $\delta\tau_k$, then update the estimation of hypocenter for step $k+1$,

$$\boldsymbol{\xi}_{k+1} = \boldsymbol{\xi}_k + \delta\boldsymbol{\xi}_k.$$

4. If $\left\|\boldsymbol{\xi}_k - \boldsymbol{\xi}_{k+1}\right\| < \varepsilon$, go to step 7; If $\left\|\boldsymbol{\xi}_k - \boldsymbol{\xi}_{k+1}\right\| > \sigma$, go to step 6.

5. If $k+1 > K$, go to step 6. Otherwise, let $k = k+1$ and go to step 2 for another iteration.
6. Output the error message: "The iteration diverges." and stop.
7. Update the estimation of origin time for step $k+1$,

$$\tau_{k+1} = \tau_k + \delta\tau_k.$$

Output $(\boldsymbol{\xi}_{k+1}, \tau_{k+1})$ and stop. □

Once the value $(\boldsymbol{\xi}_{k+1}, \tau_{k+1})$ is output, we get the hypocenter and the origin time for the specific earthquake. Otherwise, the algorithm should be restarted with different initial value of hypocenter $\boldsymbol{\xi}_0$ until the convergent result is obtained.

In this algorithm, the extra computational cost arise from solving the sub-optimization problem (22) and (23). But this part in the overall computational cost is minor. The reason is that the sub-optimization problem (22) and (23) are only one dimensional. Taking into consideration the saving from less computation of the wave equations, the total cost is reduced here. Furthermore, since the new method greatly enlarges the convergence domain, the number of initial values of hypocenter that we need to select in solving the earthquake location problem can be significantly reduced compared to the conventional method. This greatly reduces the overall computational cost.

4 NUMERICAL EXPERIMENTS

In this section, three examples are presented to demonstrate the validity of our method. And we will see the comparison between the conventional method and the new method for the earthquake location problem.

Example 4.1. Let's take the same parameters set up as in Exam 3.1. Then the real signals $d_r(t)$ and the synthetic $s(\boldsymbol{\eta}_r, t)$ can be obtained by (4), (5) and (15) for different receiver $r = 1, 2, \cdots, 20$.

Consider an earthquake occurs at hypocenter $\boldsymbol{\xi}_T = (50km, -30km)$ and origin time $\tau_T = 10s$ with dominant frequency $f_0 = 2$Hz. In Figure 5 (Up, Left), 1280 uniformly distributed grid nodes are tested as the initial hypocenter of earthquake $\boldsymbol{\xi}$ in the searching domain $[46km, 54km] \times [-35km, -25km]$ for the conventional method. This is the simplest experimental design technique (Cochran & Cox 1992), but it is enough to illustrate the effectiveness of our new method. There are

228 grid nodes converge to the correct hypocenter. Therefore, the area of the convergence domain is roughly estimated as

$$(54-46)\times((-25)-(-35))\times\frac{228}{1280}=14.3\ km^2.$$

In Figure 5 (Up, Right), 2800 uniformly distributed grid nodes are tested as the initial hypocenter of earthquake $\boldsymbol{\xi}$ in the searching domain $[10km, 90km]\times[-70km, 0km]$ for the new method. There are 1597 grid nodes converge to the correct hypocenter. Using the same formula, the area of the convergence domain is roughly estimated as $3194\ km^2$. In contrast, the convergence probability of the new method is about

$$3194\div 14.3\approx 223,$$

times that of the conventional method for this case.

From the figure, we can also see that all the tested initial hypocenter in the rectangular region $[49km, 51km]\times[-31km, -29.25km]$ converge to the correct hypocenter for the conventional method. For the new method, this rectangular region is $[38km, 62km]\times[-53.5km, -7.5km]$, its area is 315 times of the former for this case.

Consider an earthquake occurs at hypocenter $\boldsymbol{\xi}_T=(50km, -6km)$ and origin time $\tau_T=10s$ with dominant frequency $f_0=$ 2Hz. In Figure 5 (Bottom, Left), 1271 uniformly distributed grid nodes are tested as the initial hypocenter of earthquake $\boldsymbol{\xi}$ in the searching domain $[48km, 52km]\times[-11km, 0km]$ for the conventional method. There are 411 grid nodes converge to the correct hypocenter, thus the area of the convergence domain is roughly estimated as $14.2\ km^2$. In Figure 5 (Bottom, Right), 1900 uniformly distributed grid nodes are tested as the initial hypocenter of earthquake $\boldsymbol{\xi}$ in the searching domain $[0km, 100km]\times[-38km, 0km]$ for the new method. There are 740 grid nodes converge to the correct hypocenter, thus the area of the convergence domain is roughly estimated as $1480\ km^2$. In contrast, the convergence probability of the new method is about 104 times that of the conventional method for this case.

From the figure, we can also see that all the tested initial hypocenter in the rectangular region $[49.25km, 50.75km]\times[-7.95km, -4.35km]$ converge to the correct hypocenter for the conven-

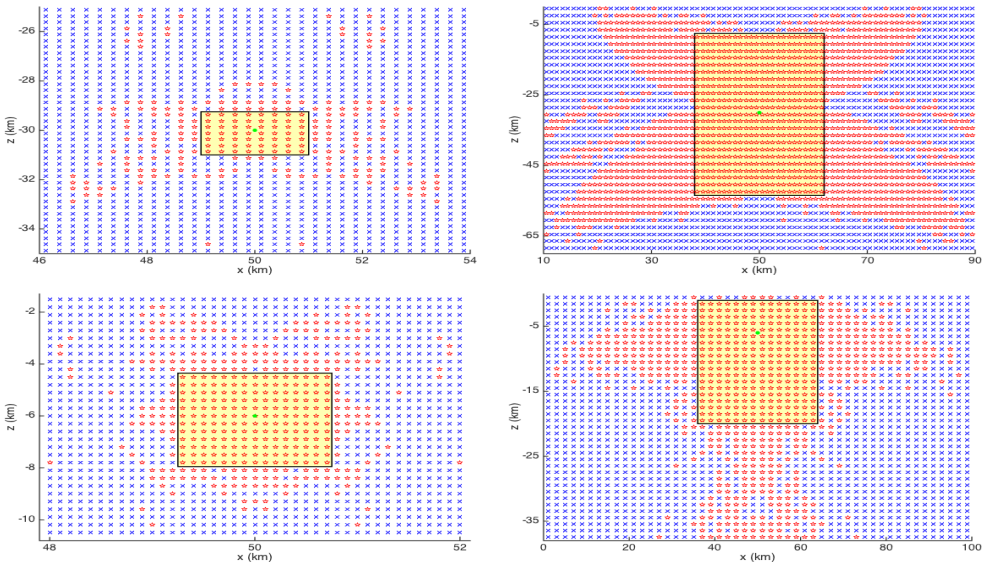

Figure 5. Illustration of the Exam 4.1. The green point is the real hypocenter. The red pentagram and the blue x-mark indicate the initial hypocenter at this location converge and misconvergence to the real hypocenter respectively. Left: the conventional method; Right: the new method. Up figures for deep earthquake $\boldsymbol{\xi}_T = (50km, -30km)$ and Bottom figures for shallow earthquake $\boldsymbol{\xi}_T = (50km, -6km)$. In the light yellow rectangular region, all the tested initial hypocenter converge to the correct hypocenter.

tional method. For the new method, this rectangular region is $[36km, 64km] \times [-20km, -1km]$, its area is 98 times of the former for this case.

Considering all of the above, we note that the new method works better for the deep earthquake rather than the shallow earthquake. One explanation is that the convergence domain is nearly symmetric about the earthquake hypocenter. But it doesn't hold for shallow earthquake in z direction since selecting the initial hypocenter above the surface is non-physical. This discussion also applies to the following examples. □

Example 4.2. Consider the two-layer model in the bounded domain $[0km, 100km] \times [-40km, 0km]$, the wave speed is

$$c(x,z) = \begin{cases} 5.2 - 0.06z + 0.2\sin\frac{\pi x}{25}, & -15km \le z \le 0km, \\ 6.2 + 0.2\sin\frac{\pi x}{25}, & -40km \le z < -15km, \end{cases}$$

for depth earthquake and

$$c(x,z) = \begin{cases} 5.2 - 0.05z + 0.2\sin\frac{\pi x}{25}, & -20km \le z \le 0km, \\ 6.8 + 0.2\sin\frac{\pi x}{25}, & -40km \le z < -20km, \end{cases}$$

for shallow earthquake. The unit is 'km/s'. We use the finite difference scheme (Dablain 1986; Wang et al. 2012; Yang et al. 2003; Yang et al. 2004; Yang et al. 2006) to solve the acoustic wave equation (1) with initial condition (2). The problem can also be solved by other numerical methods, e.g. finite element methods (Lysmer & Drake 1972; Marfurt 1984), the spectral element method (Kim et al. 2011; Liu et al. 2004) and the discontinuous Galerkin method (He et al. 2014; He et al. 2015). The reflection boundary condition is used on the earth's surface, and the perfectly matched layer (Komatitsch & Tromp 2003; Ma et al. 2015) is used for other boundaries. The delta function $\delta(\boldsymbol{x}-\boldsymbol{\xi})$ in the wave equation (1) is discretized using the techniques proposed in (Wen 2008).

$$\delta(x)=\begin{cases}\frac{1}{h}\left(1-\frac{5}{4}\left|\frac{x}{h}\right|^2-\frac{35}{12}\left|\frac{x}{h}\right|^3+\frac{21}{4}\left|\frac{x}{h}\right|^4-\frac{25}{12}\left|\frac{x}{h}\right|^5\right), & |x|\le h,\\ \frac{1}{h}\left(-4+\frac{75}{4}\left|\frac{x}{h}\right|-\frac{245}{8}\left|\frac{x}{h}\right|^2+\frac{545}{24}\left|\frac{x}{h}\right|^3-\frac{63}{8}\left|\frac{x}{h}\right|^4+\frac{25}{24}\left|\frac{x}{h}\right|^5\right), & h<|x|\le 2h,\\ \frac{1}{h}\left(18-\frac{153}{4}\left|\frac{x}{h}\right|+\frac{255}{8}\left|\frac{x}{h}\right|^2-\frac{313}{24}\left|\frac{x}{h}\right|^3+\frac{21}{8}\left|\frac{x}{h}\right|^4-\frac{5}{24}\left|\frac{x}{h}\right|^5\right), & 2h<|x|\le 3h,\\ 0, & |x|>3h.\end{cases}$$

There are 20 equidistant receivers on the surface

$$\boldsymbol{\eta}_r=(x_r,z_r)=(5r-2.5km,0),\quad r=1,2,\cdots,20.$$

Since the hypocenter of earthquake is not far from the receiver stations, we only use the direct wave to locate the earthquake.

Consider an earthquake occurs below the medium interface $\boldsymbol{\xi}_T=(50km,-20km)$ and origin time $\tau_T=10s$ with dominant frequency $f_0=2$Hz (see Figure 6 Up). In Figure 7 (Up, Left), 600 uniformly distributed grid nodes are tested as the initial hypocenter of earthquake $\boldsymbol{\xi}$ in the searching domain $[44km,56km]\times[-26km,-10km]$ for the conventional method. There are 210 grid nodes converge to the correct hypocenter, thus the area of the convergence domain is roughly estimated as $67.2\ km^2$. In Figure 7 (Up, Right), 1480 uniformly distributed grid nodes are tested as the initial hypocenter of earthquake $\boldsymbol{\xi}$ in the searching domain $[10km,90km]\times[-40km,0km]$ for the new method. There are 881 grid nodes converge to the correct hypocenter, thus the area of the convergence domain is roughly estimated as $1905\ km^2$. In contrast, the convergence probability of the new method is about 28.3 times that of the conventional method for this case.

From the figure, we can also see that all the tested initial hypocenter in the rectangular region $[48.95km, 51.05km] \times [-14.5km, -1.5km]$ converge to the correct hypocenter for the conventional method. For the new method, this rectangular region is $[33km, 67km] \times [-33.5km, -5.5km]$, its area is 46.0 times of the former for this case.

Consider an earthquake occurs above the medium interface $\boldsymbol{\xi}_T = (50km, -6km)$ and origin time $\tau_T = 10s$ with dominant frequency $f_0 = 2$Hz (see Figure 6 Bottom). In Figure 7 (Bottom, Left), 441 uniformly distributed grid nodes are tested as the initial hypocenter of earthquake $\boldsymbol{\xi}$ in the searching domain $[47km, 53km] \times [-21km, -1km]$ for the conventional method. There are 216 grid nodes converge to the correct hypocenter, thus the area of the convergence domain is roughly estimated as $58.8\ km^2$. In Figure 7 (Bottom, Right), 1344 uniformly distributed grid nodes are tested as the initial hypocenter of earthquake $\boldsymbol{\xi}$ in the searching domain $[8km, 92km] \times [-25km, 0km]$ for the new method. There are 592 grid nodes converge to the correct hypocenter, thus the area of the convergence domain is roughly estimated as $925\ km^2$. In contrast, the convergence probability of the new method is about 15.7 times that of the conventional method for this case.

From the figure, we can also see that all the tested initial hypocenter in the rectangular region $[47.75km, 52.25km] \times [-22.3km, -17.7km]$ converge to the correct hypocenter for the conventional method. For the new method, this rectangular region is $[38km, 62km] \times [-12.6km, 0km]$, its area is 11.1 times of the former for this case. □

Example 4.3. Consider the velocity model consisting of the crust and the mantle, containing an undulated Moho discontinuity and a subduction zone with a thin low velocity layer atop a fast velocity layer (Tong et al. 2016), see Figure 8 for illustration. The computational domain is

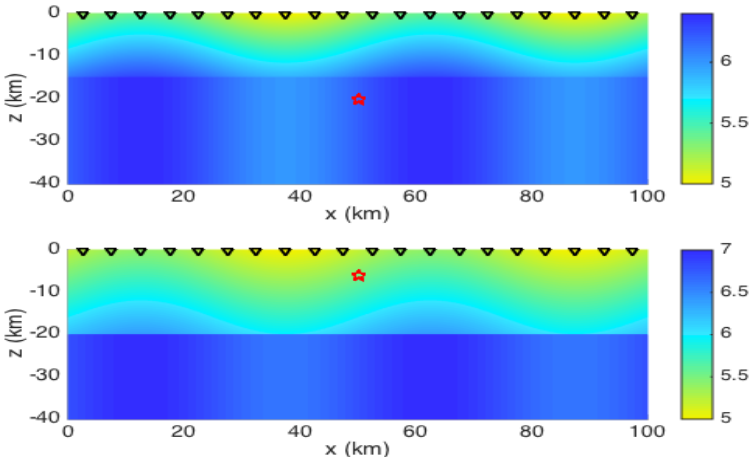

Figure 6. Velocity models in Example 4.2. The red pentagrams show the hypocenter of earthquake and the black triangles indicate the receiver stations.

$[0km, 200km] \times [-200km, 0km]$, and the wave speed is

$$c(x,z) = \begin{cases} 5.5, & -33 - 2.5\sin\frac{\pi x}{40} \le z < 0, \\ 7.8, & -45 - 0.4x \le z < -33 - 2.5\sin\frac{\pi x}{40}, \\ 7.488, & -60 - 0.4x \le z < -45 - 0.4x. \\ 8.268, & -100 - 0.4x \le z < -60 - 0.4x. \\ 7.8, & \text{others}. \end{cases}$$

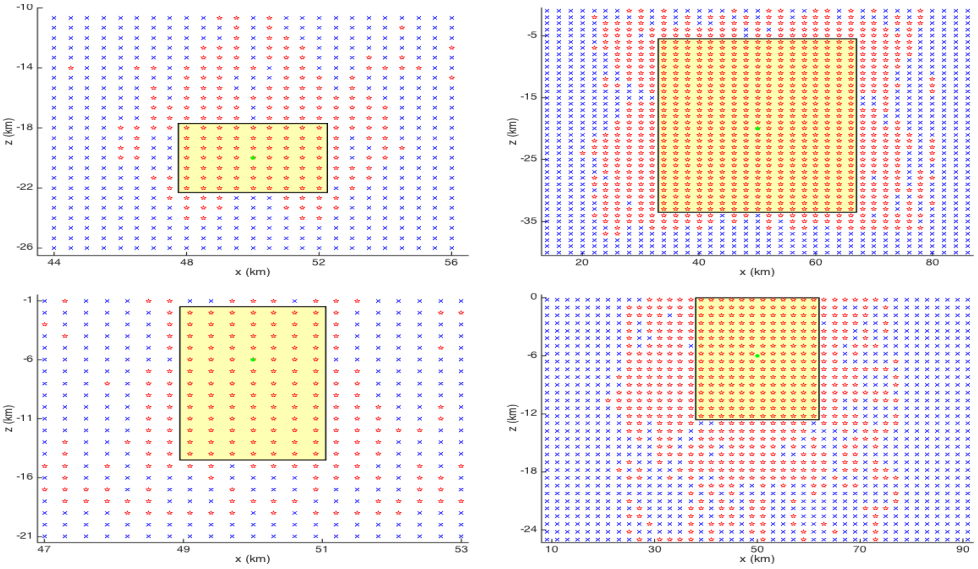

Figure 7. Illustration of the Exam 4.2. The green point is the real hypocenter. The red pentagram and the blue x-mark indicate the initial hypocenter at this location converge and misconvergence to the real hypocenter respectively. Left: the conventional method; Right: the new method. Up figures for deep earthquake $\boldsymbol{\xi}_T = (50km, -20km)$ and Bottom figures for shallow earthquake $\boldsymbol{\xi}_T = (50km, -6km)$. In the light yellow rectangular region, all the tested initial hypocenter converge to the correct hypocenter.

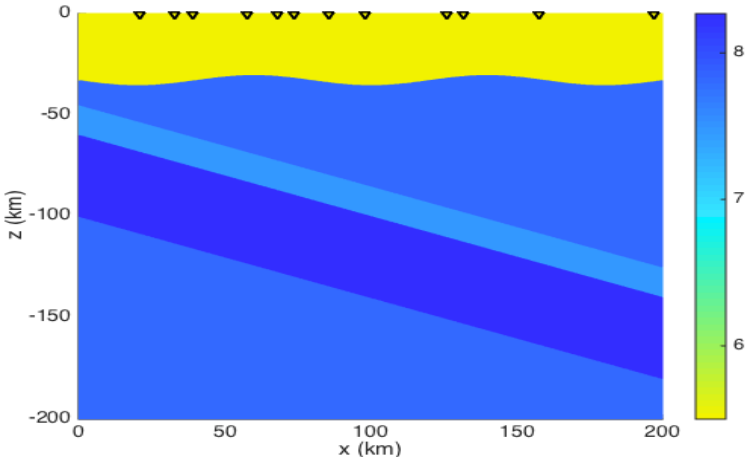

Figure 8. Velocity model in Example 4.3. The black triangles indicate the receiver stations.

with unit 'km/s'. We consider the same set-up as in Exam 4.2, e.g. the forward scheme, the boundary conditions and the discretized delta function. There are 12 receivers $\boldsymbol{\eta}_r = (x_r, z_r)$ on the surface with $z_r = 0$, their horizontal positions are randomly given, see Table 1 for details. In this example, we still only use the directive wave to locate the earthquake. In real world, region with the similar velocity model is always seismogenic zone (Tong et al. 2011). Earthquakes in this kind of region can occur in the crust, in the subduction zone or in the mantle (Tong et al. 2012). Complex velocity structure makes source location very difficult.

We firstly investigate the case that the earthquake occurs in the mantle but the initial hypocenter of the earthquake is chosen in the subduction zone, and its contrary case. In Figure 9, we can see the convergent history. The second case is that the earthquake occurs in the mantle but the initial hypocenter of the earthquake is chosen in the crust. The convergent history can be seen in Figure 10. From these tests, we can observes nice convergent result of the new method, even though the real and initial hypocenter of the earthquakes are far from each other. □

Table 1. Example 4.3: the horizontal positions of receivers, with unit 'km'.

r	1	2	3	4	5	6	7	8	9	10	11	12
z_r	21	33	39	58	68	74	86	98	126	132	158	197

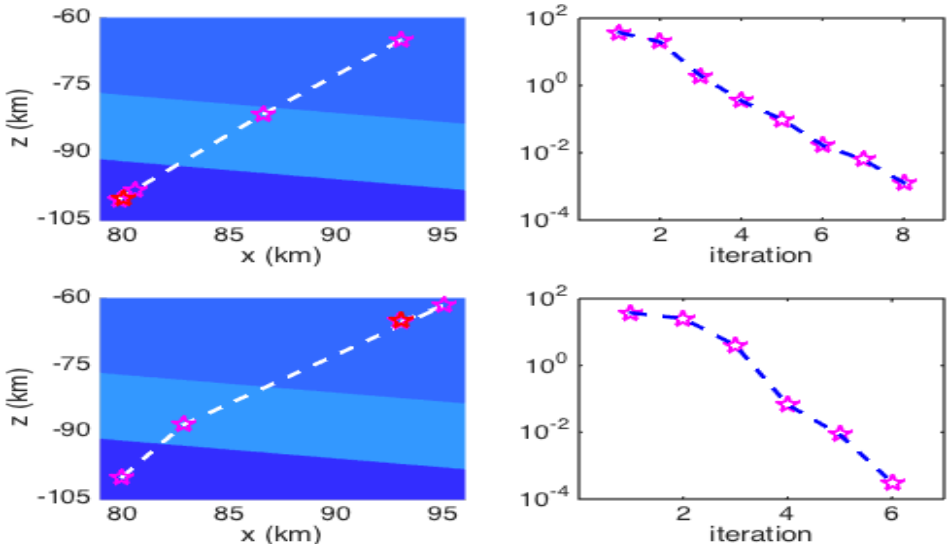

Figure 9. Convergent history of the first case in Example 4.3, from initial hypocenter in the subduction zone to the real hypocenter in the mantle (Up) and its contrary case (Bottom). Left: the convergent trajectories; Right: the absolute errors with respect to iteration step between the real and computed hypocenter of the earthquake.

5 CONCLUSION AND DISCUSSION

The main contribution in this paper is that convergence domain of the waveform based earthquake location method has been greatly expanded. Accordingly to the numerical evidence presented earlier, the convergence domain has been enlarged $10 \sim 300$ times in the two test problems. This means that even from the relatively poor initial values of earthquake hypocenter, our method is also likely to convergence to the correct results with high accuracy.

We have to explain that this paper focuses on the development of new method. For practical

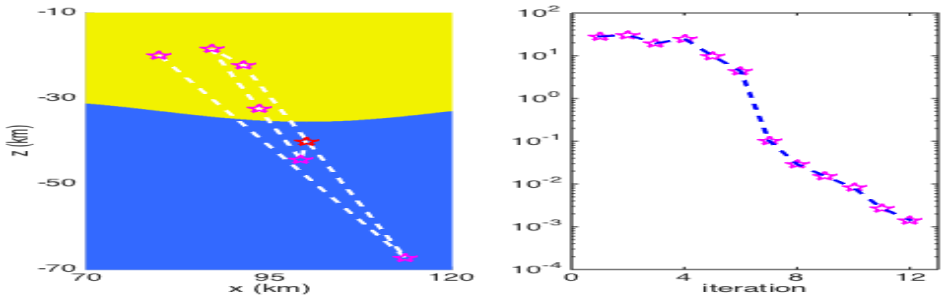

Figure 10. Convergent history of the second case in Example 4.3, from initial hypocenter in the crust to the real hypocenter in the mantle. Left: the convergent trajectory; Right: the absolute errors with respect to iteration step between the real and computed hypocenter of the earthquake.

three-dimensional problem, we believe that the new method is also applicable. We are investigating this approach. We hope this can be reported in an independent publication in the near future.

ACKNOWLEDGMENTS

This work was supported by the National Nature Science Foundation of China (Grant Nos 41230210, 41390452). Hao Wu was also partially supported by the National Nature Science Foundation of China (Grant No 11101236) and SRF for ROCS, SEM. The authors are grateful to Prof. Shi Jin for his helpful suggestions and discussions that greatly improve the presentation. Hao Wu would like to thank Prof. Ping Tong for his valuable comments.

REFERENCES

Aki, K. & Richards, P.G., 1980. *Quantitative Seismology: Theory and Methods volume II*, W.H. Freeman & Co (Sd).

Alkhalifah, T., 2010. Acoustic wavefield evolution as a function of source location perturbation, *Geophys. J. Int.*, **183**(3), 1324-1331.

Cochran, W.G. & Cox, G.M., 1992. *Experimental Designes (Second Edition)*, Wiley.

Dablain, M.A., 1986. The application of high-order differencing to the scalar wave equation, *Geophysics*, **51**(1), 54-66.

Engquist, B. & Froese, B.D., 2014. Application of the Wasserstein metric to seismic signals, *Commun. Math. Sci.*, **12**(5), 979-988.

Engquist, B. & Runborg, O., 2003. Computational high frequency wave propagation, *Acta Numer.*, **12**, 181-266.

Engquist, B., Froese, B.D. & Yang, Y.N., 2016. Optiaml transport for seismic full waveform inversion, *preprint*.

Evans, L.C., 2010. *Partial Differential Equations Second Edition*, American Mathematical Society.

Ge, M.C., 2003a. Analysis of source location algorithms Part I: Overview and non-iterative methods, *J. Acoust. Emiss.*, **21**, 14-28.

Ge, M.C., 2003b. Analysis of source location algorithms Part II: Iterative methods, *J. Acoust. Emiss.*, **21**, 29-51.

Geiger, L., 1910. Herdbestimmung bei erdbeden ans den ankunftzeiten, *K. Gessel. Wiss. Goett.*, **4**, 331-349.

Geiger, L., 1912. Probability method for the determination of earthquake epicenters from the arrival time only, *Bull. St. Louis Univ.*, **8**, 60-71.

He, X.J., Yang, D.H. & Wu, H., 2014. Numerical dispersion and wave-field simulation of the Runge-Kutta discontinuous Galerkin method, *Chinese J. Geophys.-Chinese Ed.*, **57**(3), 906-917.

He, X.J., Yang, D.H. & Wu, H., 2015. A weighted RungeKutta discontinuous Galerkin method for wavefield modelling, *Geophys. J. Int.*, **200**, 1389-1410.

Huang, X.Y., Yang, D.H., Tong, P., Badal, J. & Liu, Q.Y., 2016. Wave equation-based reflection tomography of the 1992 Landers earthquake area, *Geophys. Res. Lett.*, **43**, 1884-1892.

Jin, S., Wu, H. & Yang, X., 2008. Gaussian Beam Methods for the Schrödinger Equation in the Semi-classical Regime: Lagrangian and Eulerian Formulations, *Commun. Math. Sci.*, **6**(4), 995-1020.

Jin, S., Wu, H. & Yang, X., 2011. Semi-Eulerian and High Order Gaussian Beam Methods for the Schrödinger Equation in the Semiclassical Regime, *Commun. Comput. Phys.*, **9**(3), 668-687.

Kim, Y.H., Liu, Q.Y. & Tromp, J., 2011. Adjoint centroid-moment tensor inversions, *Geophys. J. Int.*, **186**, 264-278.

Komatitsch, D. & Tromp, J., 2003. A perfectly matched layer absorbing boundary condition for the second-order seismic wave equation, *Geophys. J. Int.*, **154**, 146-153.

Lee, W.H.K. & Stewart, S.W., 1981. *Principles and Applications of Microearthquake Networks*, Academic Press.

Liu, H.L., Runborg, O. & Nicolay, N.M., 2013. Error estimates for Gaussian beam superpositions, *Math. Comput.*, **82**(282), 919-952.

Liu, Q.Y. & Gu, Y.J., 2012. Seismic imagine: From classical to adjoint tomography, *Tectonophysics*, **566-567**, 31-66.

Liu, Q.Y., Polet, J., Komatitsch, D. & Tromp, J., 2004. Spectral-Element Moment Tensor Inversion for Earthquakes in Southern California, *Bull. seism. Soc. Am.*, **94**(5), 1748-1761.

Lysmer, J. & Drake, L.A., 1972. A finite element method for seismology, *Meth. Comput. Phys.*, **11**, 181-216.

Ma, X., Yang, D.H. & Song, G.J., 2015. A Low-Dispersive Symplectic Partitioned Runge-Kutta Method for Solving Seismic-Wave Equations: II. Wavefield Simulations, *Bull. seism. Soc. Am.*, **105**(2A), 657-675.

Madariaga, R., 2015. Seismic Source Theory, in *Treatise on Geophysics (Second Edition)*, pp. 51-71, ed. Gerald, S., Elsevier B.V.

Marfurt, K.J., 1984. Accuracy of finite-difference and finite-element modeling of the scalar and elastic wave equations, *Geophysics*, **49**(5), 533-549.

Milne, J., 1986. *Earthquakes and other earth movements*, New York: Appleton.

Nocedal, J. & Wright, S.J., 1999. *Numerical Optimization*, Springer.

Prugger, A.F. & Gendzwill, D.J., 1988. Microearthquake location: A nonlinear approach that makes use of a simplex stepping procedure, *Bull. seism. Soc. Am.*, **78**, 799-815.

Rawlinson, N., Pozgay, S. & Fishwick, S., 2010. Seismic tomography: A window into deep Earth, *Phys. Earth Planet. Inter.*, **178**, 101-135.

Satriano, C., Lomax, A. & Zollo, A., 2008. Real-Time Evolutionary Earthquake Location for Seismic Early Warning, *Bull. seism. Soc. Am.*, **98**(3), 1482-1494.

Tape, C., Liu, Q.Y. & Tromp, J., 2007. Finite-frequency tomography using adjoint methods - methodology and examples using membrane surface waves, *Geophys. J. Int.*, **168**, 1105-1129.

Thurber, C.H., 1985. Nonlinear earthquake location: Theory and examples, *Bull. seism. Soc. Am.*, **75**(3), 779-790.

Thurber, C.H., 2014. Earthquake, location techniques, in *Encyclopedia of Earth Sciences Series*, pp. 201-207, ed. Gupta, H.K., Springer.

Tong, P., Zhao, D.P. & Yang, D.H., 2011. Tomography of the 1995 Kobe earthquake area: comparison of finite-frequency and ray approaches, *Geophys. J. Int.*, **187**, 278-302.

Tong, P., Zhao, D.P. & Yang, D.H., 2012. Tomography of the 2011 Iwaki earthquake (M 7.0) and Fukushima nuclear power plant area, *Solid Earth*, **3**, 43-51.

Tong, P., Chen, C.W., Komatitsch, D. & Liu, Q.Y., 2014a. High-resolution seismic array imaging based on an SEM-FK hybrid method, *Geophys. J. Int.*, **197**, 369-395.

Tong, P., Zhao, D., Yang, D., Yang, X., Chen, J. & Liu, Q., 2014b. Wave-equation-based travel-time seismic tomography - Part 1: Method, *Solid Earth*, **5**, 1151-1168.

Tong, P., Zhao, D., Yang, D., Yang, X., Chen, J. & Liu, Q., 2014c. Wave-equation-based travel-time seismic tomography - Part 2: Application to the 1992 Landers earthquake (M_w7.3) area, *Solid Earth*, **5**, 1169-1188.

Tong, P., Yang, D.H., Liu, Q.Y., Yang, X. & Harris, J., 2016. Acoustic wave-equation-based earthquake location, *Geophys. J. Int.*, **205**(1), 464-478.

Tromp, J., Tape, C. & Liu, Q.Y., 2005. Seismic tomography, adjoint methods, time reversal and banana-doughnut kernels, *Geophys. J. Int.*, **160**, 195-216.

Waldhauser, F. & Ellsworth, W.L., 2000. A double-difference earthquake location algorithm: Method and application to the northern Hayward Fault, California, *Bull. seism. Soc. Am.*, **90**(6), 1353-1368.

Wang, M.X., Yang, D.H. & Song, G.J., 2012. Semi-analytical solutions and numerical simulations of 2D SH wave equation, *Chinese J. Geophys.-Chinese Ed.*, **55**(3), 914-924.

Wen, X., 2008. High Order Numerical Quadratures to One Dimensional Delta Function Integrals, *SIAM J. Sci. Comput.*, **30**(4), 1825-1846.

Wu, H. & Yang, X., 2013. Eulerian Gaussian beam method for high frequency wave propagation in the reduced momentum space, *Wave Motion*, **50**(6), 1036-1049.

Yang, D.H., Lu, M., Wu, R.S. & Peng, J.M., 2004. An Optimal Nearly Analytic Discrete Method for 2D Acoustic and Elastic Wave Equations, *Bull. seism. Soc. Am.*, **94**(5), 1982-1991.

Yang, D.H., Peng, J.M., Lu, M. & Terlaky, T., 2006. Optimal Nearly Analytic Discrete Approximation to the Scalar Wave Equation, *Bull. seism. Soc. Am.*, **96**(3), 1114-1130.

Yang, D.H., Teng, J.W., Zhang, Z.J. & Liu, E.R., 2003. A Nearly Analytic Discrete Method for Acoustic and Elastic Wave Equations in Anisotropic Media, *Bull. seism. Soc. Am.*, **93**(2), 882-890.